Argonne
NATIONAL LABORATORY

ANL-07/20

In Situ Electrochemical and X-ray Characterization and Fabrication of Thin-Film Oxygen Electrodes for Solid Oxide Electrolysis Cells

Nuclear Engineering Division

About Argonne National Laboratory

Argonne is a U.S. Department of Energy laboratory managed by UChicago Argonne, LLC under contract DE-AC02-06CH11357. The Laboratory's main facility is outside Chicago, at 9700 South Cass Avenue, Argonne, Illinois 60439. For information about Argonne, see www.anl.gov.

Availability of This Report

This report is available, at no cost, at http://www.osti.gov/bridge. It is also available on paper to the U.S. Department of Energy and its contractors, for a processing fee, from:

U.S. Department of Energy
Office of Scientific and Technical Information
P.O. Box 62
Oak Ridge, TN 37831-0062
phone (865) 576-8401
fax (865) 576-5728
reports@adonis.osti.gov

ANL-07/20

In Situ Electrochemical and X-ray Characterization and Fabrication of Thin-Film Oxygen Electrodes for Solid Oxide Electrolysis Cells

Part I: Electrochemical and X-ray Characterization of Solid-Oxide Electrolysis Cell Oxygen Electrodes on Electrolyte Substrates

by
B. Yildiz,[1] K.-C. Chang,[2] D.J. Myers,[3] H. You,[2] J.D. Carter[3]
[1]Nuclear Engineering Division, Argonne National Laboratory
[2]Materials Science Division, Argonne National Laboratory
[3]Chemical Engineering Division, Argonne National Laboraotory

Part II: Progress Towards the Atomic Layer Deposition of Lanthanum Strontium Manganate

by
J.W. Elam,[1] D.A. Honegger,[1] J.A. Libera,[1] and M.J. Pellin[2]
[1]Energy Systems Division, Argonne National Laboratory
[2]Materials Science Division, Argonne National Laboratory

May 15, 2007

Part I: Electrochemical and X-ray Characterization of Solid-Oxide Electrolysis Cell Oxygen Electrodes on Electrolyte Substrates

Bilge Yildiz, Kee-Chul Chang, Deborah J. Myers, Hoydoo You, J. David Carter

Part II: Progress Towards the Atomic Layer Deposition of Lanthanum Strontium Manganate

Jeffrey W. Elam, David A. Honegger, Joseph A. Libera, and Michael. J. Pellin

Part I: Electrochemical and X-ray Characterization of Solid-Oxide Electrolysis Cell Oxygen Electrodes on Electrolyte Substrates

Bilge Yildiz, Kee-Chul Chang, Deborah J. Myers, Hoydoo You, J. David Carter

ABSTRACT

The governing reaction mechanisms, and the electrode and electrolyte material compositions and structures, that controls the efficiency and durability of the solid oxide electrolysis cells (SOEC) need to be identified and well-understood for a significant improvement in nuclear hydrogen production using high temperature steam electrolysis. ANL conducted experimental analysis of SOEC electrolyte and electrodes to progress in this objective.

Our study on the oxygen electrode focused on specifically the effect of electrode crystal structure on its electrochemical performance, and the evolution of the electronic and structural properties of the electrodes while under electrochemical conditions and high temperature. We found through electrochemical impedance spectroscopy experiments that, while different crystal orientations in $La_{0.8}Sr_{0.2}MnO_{3+d}$ (LSM) show different initial performance and different electrochemical activation under SOEC conditions, a good mixed ionic electronic conductor $La_{0.8}Sr_{0.2}CoO_{3+d}$ (LSC) does not seem to exhibit similar variations. Our *in-situ* x-ray and electrochemical measurements at the Advanced Photon Source of ANL have identified the chemical states of the A-site elements of the doped lanthanum manganite electrodes. We found that the changes in the concentration and in the electronic state of the La and Sr (the A-site elements of the perovskite) occurring only at the top air-electrode film interface can be responsible from the electrochemical improvement of the SOEC anode under DC current. Our observation related to the La chemical state change is unexpected and probably unique to the electrochemical current-conditioning.

TABLE OF CONTENTS

1. Introduction and Objectives

Solid-oxide electrolysis cells (SOECs) are a potential route to low-cost hydrogen production by high-temperature steam electrolysis linked to a nuclear power plant. Indeed, through the efforts of the Department of Energy Nuclear Hydrogen Initiative work led by Idaho National Laboratory, SOECs have been developed that are already producing hydrogen in the laboratory. One of the remaining hurdles for SOECs that prevents them from being readily adopted for the commercial production of hydrogen is the high cost of the hydrogen produced. Most of this cost comes from the SOECs themselves, rather than from the ancillary plant equipment needed to handle feed streams and output. Significant SOEC cost reductions related to raw material costs, manufacturing costs, stack lifetimes, and cell efficiency will be needed for high-temperature steam electrolysis to become a competitive source of hydrogen. The objective of this joint University of Nevada-Las Vegas (UNLV) and Argonne National Laboratory (Argonne) project is to address several of these key technical issues to reduce the overall cost of hydrogen produced through SOECs.

Energy losses in SOECs come from the inherent electrochemistry of the electrodes and the electrolyte and from the degradation of electrochemical properties over the life of the cell, similar to the case with the solid oxide fuel cells (SOFCs). Reducing these losses would improve the hydrogen output per unit area of the cells, reduce the SOEC size, and extend the life of the cells. It is important that the source of the energy losses be addressed and improvements be made for all three components of a cell: the oxygen electrode, the hydrogen electrode, and the electrolyte.

Published data show that for solid oxide cells at 800°C the area-specific resistances are 0.1 Ω-cm^2 for the hydrogen electrode, 0.1 Ω-cm^2 for the yttria-stabilized zirconia (YSZ) thin-film electrolyte (10μm thick), and 0.2 Ω-cm^2 for the oxygen electrode[1]. The oxygen electrode is the most significant source of irreversibility. Similar results have been found for the Ceramatec-based SOECs in the Idaho National Laboratory-led project, which use much thicker electrolytes (150 microns) made with scandia-stabilized zirconia (SSZ). Oxygen electrode overpotential was found to be twice that of the hydrogen electrode and that of the thick electrolyte. Optimizing the properties of the electrodes, then, can greatly improve cell performance. Unfortunately, there exists only limited understanding of the underlying reaction mechanisms related to performance of electrode-electrolyte systems. Specifically, little is known about the relationship between the SOEC electrochemistry and electrode surface and electrode/electrolyte interface structure and composition. Progress in developing improved SOECs would significantly benefit from a systematic study and understanding of these relationships. Such study should encompass the molecular level characterization and modeling of the relations between the electrode performance (reaction rates) and the electrode/electrolyte structures and compositions.

Project Objectives and Approach

The overall goal of the collaborative Argonne/University of Nevada-Las Vegas project is to address key fundamental and technical issues through understanding the governing SOEC properties and mechanisms, utilize this knowledge in making more efficient and durable SOEC materials, and consequently reduce the cost of hydrogen production through high-temperature steam electrolysis. Improving the energy efficiency and durability of SOECs will come through three main objectives of the overall project:

1. Demonstrate the manufacture and use of thin, pinhole-free, adherent electrolytes through atomic layer deposition (ALD) techniques in order to decrease electrolyte-related energy losses. In this way, electrolytes as thin as 100 nm may be possible, a reduction of three orders of magnitude from SOECs currently being tested by the INL-led effort. Such thin electrolytes would greatly reduce electrolyte energy losses.
2. Identify optimal interface composition, structures, and phases for oxygen electrode materials in order to decrease energy losses due to poor electrode kinetics. In addition, long-term electrode degradation mechanisms will be identified, as well as ways to mitigate that degradation.
3. Identify the operating conditions (e.g., temperature and pressure) and gas composition limits (the H_2/H_2O ratio) at the hydrogen electrode to avoid catalytic and mechanical degradation related to nickel oxidation in the Ni-YSZ cermet.

The second part of this report describes the progress towards accomplishing the first objective of the project. This first part of the report presents the electrochemical characterization of the thin film oxygen electrodes fabricated by pulsed laser deposition (PLD) approach, and the progress towards identifying favorable chemical, structural and morphological properties of the SOEC oxygen electrodes. The effort this year focused on the oxygen electrode, specifically the effect of electrode crystal structure and morphology on its electrochemical performance, and the evolution of the electronic and structural properties of the electrodes while under electrochemical conditions and high temperature.

2. Analysis

2.1. Effect of Crystal Structure on Electrochemical Impedance

2.1.1. Objectives

The effect of the electrode crystal structure on the oxygen reaction kinetics of SOECs and SOFCs has not been investigated previously and remains an unknown, although it can significantly influence the electrochemical activity of the electrode. In order to identify the favorable crystal structure for enhanced surface exchange and bulk diffusion of oxygen at the SOEC oxygen electrodes, we have fabricated model dense, thin-film perovskite oxygen electrodes on single crystal YSZ electrolyte substrates. Dense oxygen electrodes allow precise control of the surface, interface, and geometric properties, which allow one to probe the electrode and electrolyte surfaces using x-ray techniques which are discussed in later sections of this report. The YSZ substrates were single crystals cut at the (100) plane and polished to 0.5nm roughness. The use of polished single crystal substrates enhanced the x-ray reflectivity of the substrates which enabled x-ray measurements of the LSM films at grazing incident angles allowing sensitivity to the electrode-air interface. It also allows deposition of crystallographically oriented films with respect to the substrate. The thin-film model electrodes were deposited on the YSZ substrates using pulsed laser deposition, and were patterned to have a reference electrode for measurements in a 3-electrode configuration. Use of a reference electrode allows separation of the polarization arising from the electrode of interest (working electrode) and the counter electrode. Platinum was painted and sintered on the opposite side of the YSZ as a counter electrode.

2.1.2. Results and Discussion

Here we report our findings on the comparison of 100nm-thick dense thin-film $La_{0.8}Sr_{0.2}MnO_{3+d}$ (LSM) and $La_{0.8}Sr_{0.2}CoO_{3+d}$ (LSC) electrodes on single crystal YSZ (100) electrolyte. The samples were deposited under two conditions: (1) T=700C, P=200mTorr, f=10Hz, (2) T=780C, P=25mTorr, f=5Hz. The 2nd set of conditions led to expitaxial growth of the LSM films, while this was not confirmed for the LSC films. The out-of-plane crystallographic orientation of the epitaxial LSM electrode film was found to be (110). The total electrochemical impedance (in terms of area specific resistance, ASR) of these electrodes under 10mV DC anodic bias is shown in Figure 1. The thick YSZ electrolyte contributes partially to the measured ASR. In FY06, we found that the performance of the two structures for LSM are comparable at and above 800°C, while the non-epitaxial film shows better activity for the oxygen evolution reaction below 800°C. This indicates that the surface exchange and/or bulk diffusion properties of the two different structures of LSM are clearly different. A specific crystal structure present in the non-epitaxial LSM makes this electrode more active as an oxygen electrode especially at lower temperatures. The dissimilar dependence of total impedance on temperature for the two cases also implies that different processes (with dissimilar activation energies of 1.24eV for the No-Epitaxy and 2.04eV for the Epitaxial (110)) are controlling the oxygen evolution kinetics at LSM as an SOEC anode. In addition, we found that the performance of these two different LSM structures vary differently when subject to representative SOEC anodic current densities, as shown in Figure 2. The electrochemical activation of the non-epitaxial LSM electrode is significantly stronger than the (110) oriented LSM film electrode, yielding a more efficient electrode structure. On the other hand, dense thin-film LSC electrodes prepared under the same conditions as the non-epitaxial and epitaxial LSM electrodes do not show significant differences in initial electrochemical behavior and in their electrochemical activation under DC polarization, as shown in Figure 3 and Figure 4. The effective activation energy for results shown in Figure 3 is 1.85eV and 1.79eV. This value is close to that reported for surface exchange of oxygen on LSC, and doesn't seem to change with drastically different deposition conditions used in this comparison. If the deposition conditions influence the bulk diffusion properties through strain relationships, the relative effect of the change in the already-fast bulk oxygen diffusion in LSC may not be a significant influence on the overall impedance characteristics.

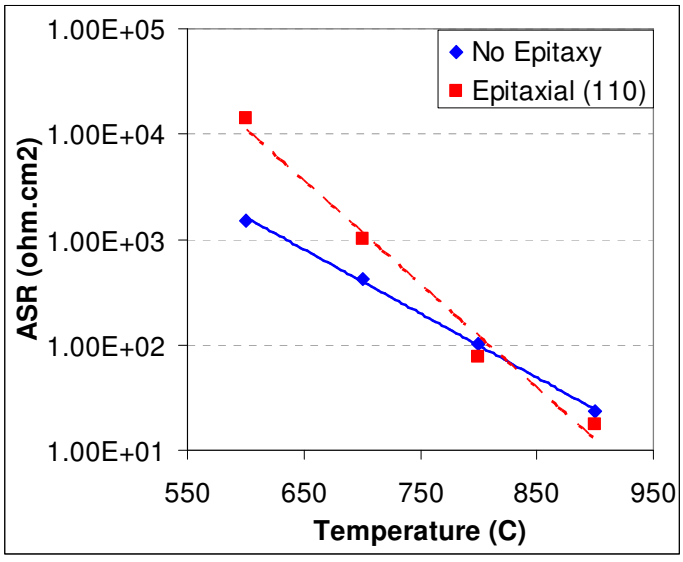

Figure 1: Total impedance of the epitaxial (110) and non-epitaxial dense thin-film LSM electrodes on single crystal YSZ (100) electrolyte, in three-electrode configuration, measured with 10mV DC bias and 10mV AC amplitude in air, as a function of temperature.

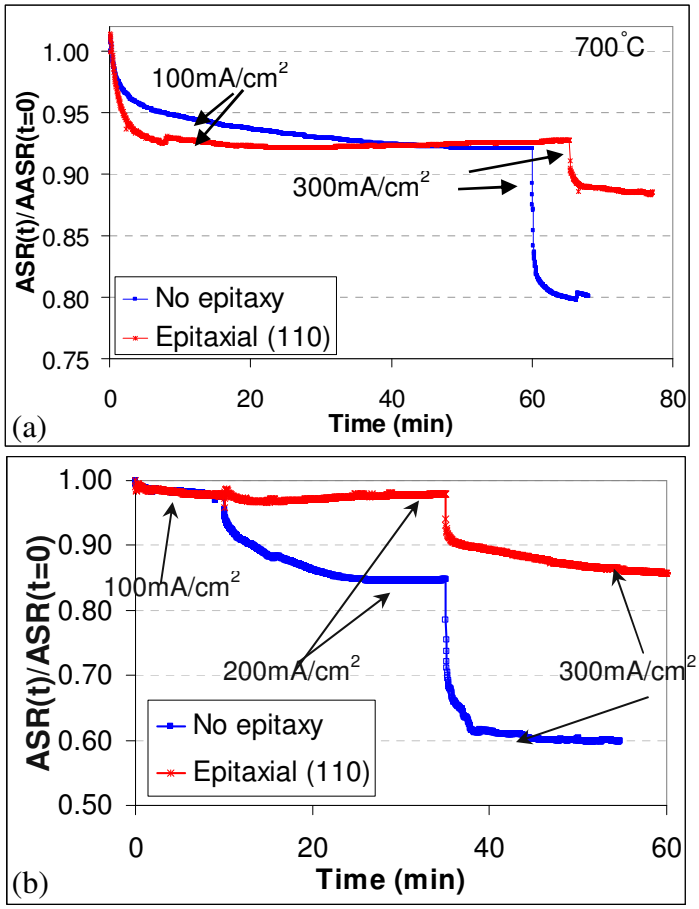

Figure 2: Relative reduction in total impedance (a) Anodic, (b) Cathodic, with time at two current densities, of the epitaxial (110) and non-epitaxial dense thin-film LSM electrodes on single crystal YSZ (100) electrolyte in air at 700°C.

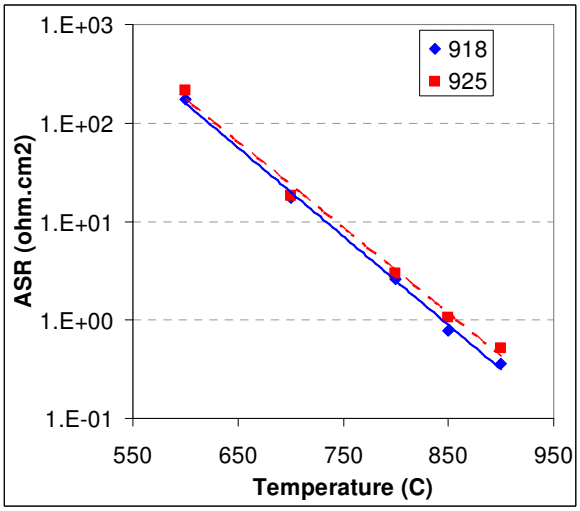

Figure 3: Total impedance of the LSC#918 and LSC#925 dense thin-film LSC electrodes on single crystal YSZ (100) electrolyte, in three-electrode configuration, 10mV DC bias, 10mV AC amplitude in air. LSC#918: Tdep= 700C, Pdep=200mTorr; LSC#925: Tdep=780C, Pdep=25mTorr.

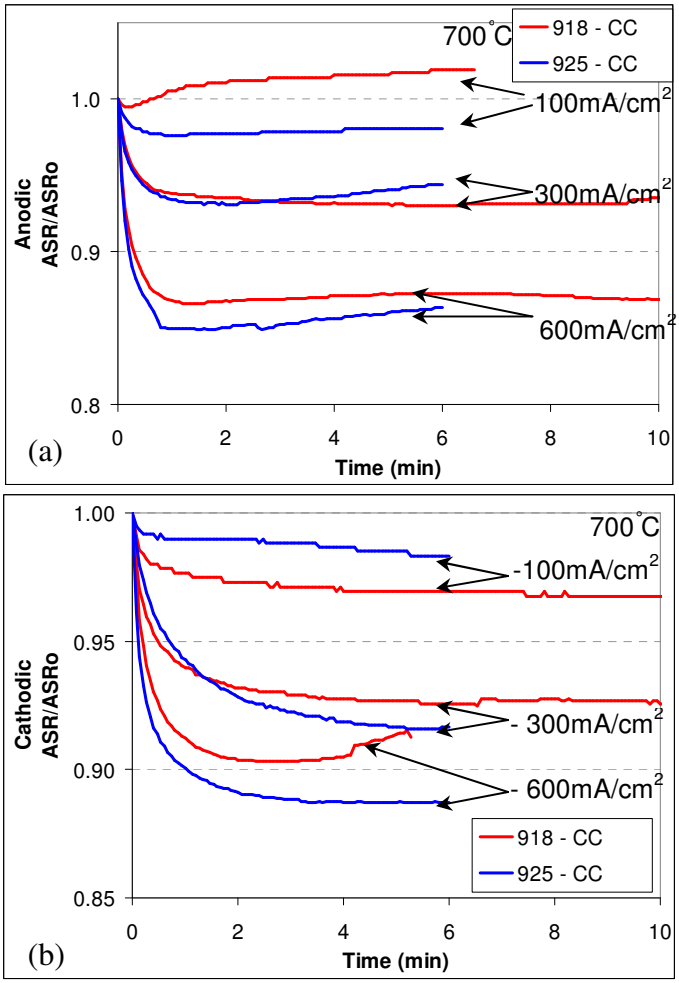

Figure 4: Relative reduction in total impedance (a) Anodic, (b) Cathodic, with time at two current densities, of the LSC#918 and LSC#925 dense thin-film LSC electrodes on single crystal YSZ (100) electrolyte in air at 700°C. LSC#918: Tdep= 700C, Pdep=200mTorr; LSC#925: Tdep=780C, Pdep=25mTorr.

2.1.2. Future Work

In order to identify and utilize the crystal structure in the non-epitaxial electrode film, we will expand our analysis to several different film orientations (other than (110)) in the manganite electrode, and in cobaltite electrodes. Due to small effective surface area of our model electrodes as compared to realistic electrodes, the electrode impedance in these experiments is large, as shown in Figure 1. However, once identified, the more active structure can be incorporated into novel electrode morphologies with high effective surface area for attaining much enhanced performance for the oxygen evolution reaction in SOECs, especially with reduced temperature operation.

2.2. In situ X-ray and Electrochemical Analysis of Oxygen Electrodes

2.2.1. Objectives

Uncertainties in our understanding of the oxygen reaction (OR) mechanism at solid oxide electrolysis and fuel cell electrodes still remain due to the complexity of the OR mechanism under steady-state conditions and to the influence of processing and operating conditions and the polarization history of the electrode. Numerous studies have shown that cathodic or anodic dc

polarization of the solid oxide cell oxygen electrodes results in a long-term or permanent enhancement of the oxygen reduction and evolution rate, and that this enhancement can remain even when returning to lower electrode polarization. This phenomenon has been termed *current-conditioning* or *activation of the electrode*. An understanding of the causes of this phenomenon can lead to better comprehension of the OR kinetics, and thus, to ways to improve its performance. In addition, the non-stationary improvement due to the activation of the electrode can provide new metrics to assess the cell performance instead of comparing only the initial stationary cell performance. *Determination of the relationship between the structure and chemical composition of the oxygen electrode and oxygen electrode/electrolyte interface under dc polarization can provide information for the rational design of electrodes with improved performance*.

Current-conditioning has been observed for several oxygen electrode materials, including platinum, lanthanum strontium manganite (LSM), lanthanum strontium manganite/yttria-stabilized zirconia composite, and lanthanum strontium iron cobaltite. Several theories have been postulated in the literature to explain the reaction rate enhancement upon dc polarization of the oxygen electrodes; however, a general and clear explanation of this phenomenon has not yet been achieved. The suggested underlying mechanism and the resulting magnitude of improvement upon activation vary significantly, even for the widely-studied electrode material LSM. Some of the theories proposed to explain the origin of the current-conditioning of LSM electrodes are reduction of the transition metal, Mn, to form oxygen ion vacancies in the perovskite lattice [1][3], removal of phases that block oxygen adsorption on the electrode surface [4][5], increase of electrode active surface or interfacial area due to roughening [6], formation of secondary phases at the electrode-electrolyte interface [7], and movement of charged species at the interfaces, such as cation diffusion [8].

All of the theories proposed for the electrode activation were based on *ex situ* electron or atomic force microscopy or *ex situ* x-ray photoelectron spectroscopy, which have limited usefulness for characterizing buried material. Thus, to obtain information on the electrode-electrolyte interface or on material buried under the surface of the electrode, the cell must be removed from its operating atmosphere and cross-sectioned. On the other hand, *in situ* x-ray studies of the SOEC and SOFC electrodes can allow determining the governing chemical, compositional and structural processes at a fundamental level. Synchrotron-based hard x-ray techniques enable *in situ* investigation of buried material, because absorptive interactions with high energy x-rays are weak enough to permit deep penetration into most materials yet strong enough to deliver surface- or interface- sensitive information. This unique penetrability/interaction allows examination of the critical interfaces under realistic operating conditions (i.e., at high temperatures and in air).

In this work, we are reporting the *in situ* x-ray spectroscopy analysis of the electrode bulk, electrode-air interface, and the near-interface regions under realistic operating conditions of the cells. We are combining the *in situ* x-ray measurements, taken during polarization in an air atmosphere at temperatures ranging from 700 to 800°C, with simultaneous electrochemical impedance spectroscopic measurements to determine the sources of oxygen electrode activation. To the best of the authors' knowledge, this study is the first *in situ* x-ray and electrochemical analysis of the solid oxide cell electrodes; though prior *in situ* studies on low temperature fuel cell cathodes have been conducted (e.g. [9],[10]).

Model dense, thin-film doped-lanthanum manganite electrodes fabricated by pulsed laser deposition on single crystal polished yttria-stabilized zirconia (YSZ) electrolyte were used for the analysis. Electrode overpotentials under anodic and cathodic polarization were applied to achieve the

electrochemical activation. The results of the structure, composition, and impedance analyses provide input for the modeling of the electrode reaction mechanisms. The modeling is based on predicting the electrochemical impedance by simulating the kinetics of the reaction mechanisms governing the electrode and electrolyte behavior at the molecular level [11].

2.2.2. Experimental Approach

Sample preparation: Dense thin-film $La_{0.8}Sr_{0.2}MnO_{3+\delta}$ (LSM) and $La_{0.8}Sr_{0.2}CoO_{3+\delta}$ (LSC) deposited on polished single crystal YSZ with (100) orientation were used as model electrodes in our study. The thin-film electrodes were prepared using the pulsed laser deposition (PLD) technique at a substrate temperature of 700-780°C. The LSM electrodes deposited at 780°C were epitaxial with (110) out-of-plane orientation. The dense film electrodes were 10-150nm thick. Porous Pt was painted and sintered on the back side of the electrolyte as a counter electrode.

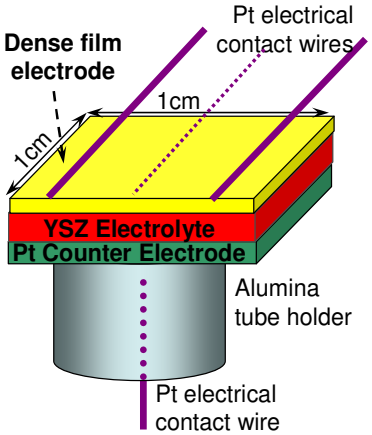

Figure 5: *In situ* electrochemical cell schematics. (Drawing not to scale.)

Electrochemical measurements: Electrochemical impedance spectroscopy (EIS), cyclic-voltammetry and potentiostatic measurements were performed using a Solartron 1255 frequency response analyzer and a Princeton Applied Research 273A potentiostat. The Pt electrical contacts were attached to the surface of the electrode on the sides and in the middle, parallel to the incoming x-ray beam in order to not obstruct the beam pathway. A 50μm-diameter fine Pt wire was attached to the middle of the dense thin-film electrode in order to ensure the electrical activation of the film at its middle region, where the x-ray beam is incident on the electrode. A schematic drawing of the *in situ* electrochemical cell is shown in Figure 5. The electrode/electrolyte samples were attached to an alumina support tube for mounting on the six-circle goniometer at the APS. The electrochemical measurements were performed in air at 700-800°C. The *in situ* electrochemical cell was heated using a parabolic infrared heater with openings drilled in the heater housing to allow access of the incoming x-rays to the sample and exit of the reflected and fluorescent x-rays.

X-ray reflectivity and spectroscopy: X-ray reflectivity and x-ray fluorescence techniques were used to examine the electrochemical cell during polarization in an air atmosphere at high temperatures. The x-ray experiments were performed at Argonne National Laboratory's Advanced Photon Source (APS), which provide highly-focused and highly-brilliant hard x-rays. X-ray reflectivity and fluorescence analysis were used for studying the structure, oxidation state, and the electron density profile of the material at the air-cathode interface, and in the bulk of the electrode. X-ray reflectivity is the ideal technique with which to study and monitor the electrode interfaces and the near-interface region. Like visible light, a beam of x-rays follows the Fresnel law of reflectivity, refracting at the interface between materials with different indices of refraction. At or near the critical angle of total

external reflection, the x-ray electric field decays rapidly inside the substrate (the electrolyte in our case) and gets strongly enhanced outside of the substrate due to the constructive interference between the incoming and reflected beams. This enhancement property allows us to measure fluorescence arising from the material (e.g., Mn, Co, La or Ni) mainly at interface of interest, but also into the electrode. Low incident angles in specular reflectivity geometry allow us to perform measurements sensitive to the bulk of the thin-film materials of our experiments. When the grazing incidence angle lower than the critical angle for a given thin-film material is used, the measurements are sensitive to approximately 1nm material at the air-electrode interface. The reflectivity measurements and the x-ray absorption spectroscopy in fluorescence mode used in our experiments is depicted in Figure 6.

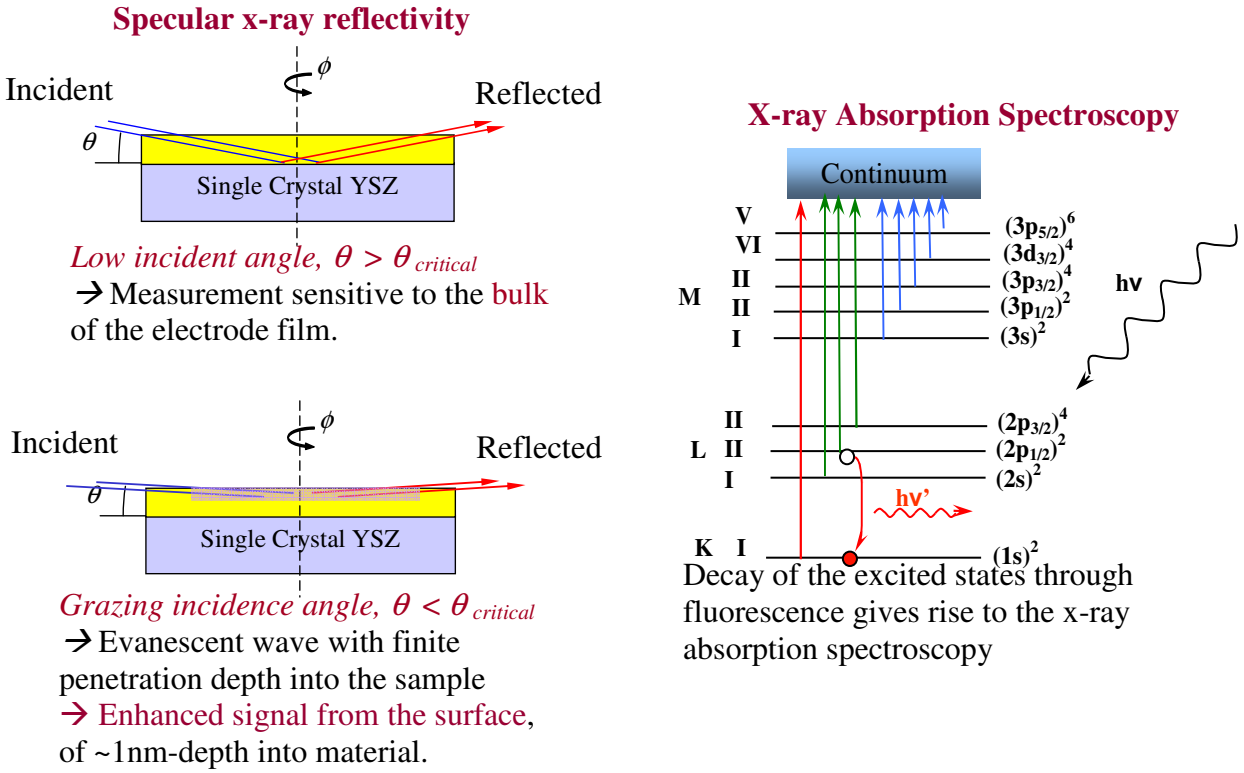

Figure 6: Schematics of grazing incidence angle X-ray reflectivity and x-ray absorption spectroscopy

X-ray reflectivity and x-ray absorption near edge spectrum (XANES) measurements of the cathode material components at its bulk and surface using the *in situ* electrochemical cell were performed at the Materials Research Collaborative Access Team (MR-CAT) insertion device beam-line at the APS. The *in situ* electrochemical setup and the incident x-ray beam path are shown in Figure 7.

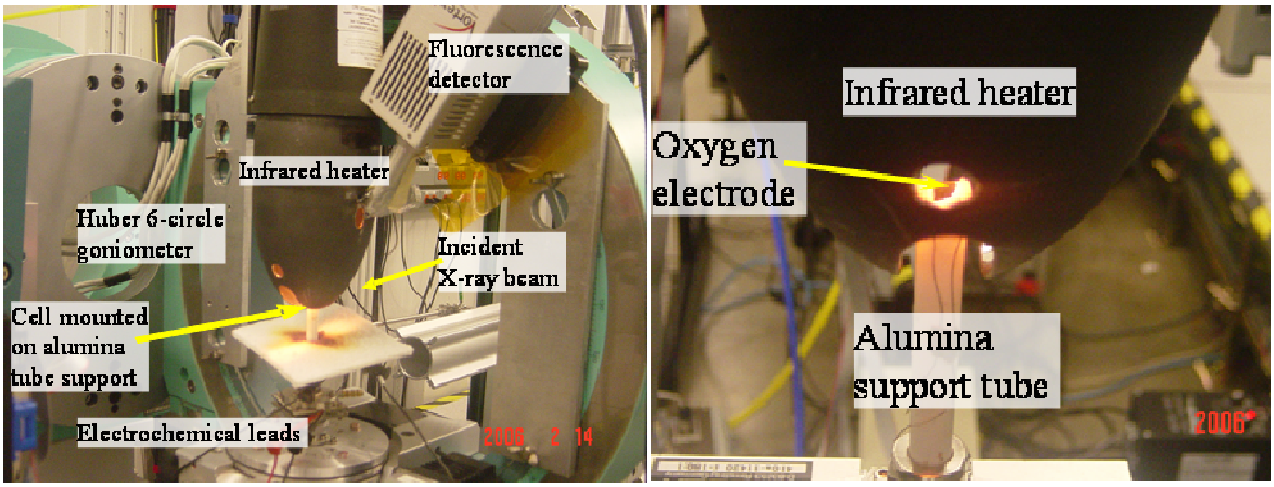

Figure 7: The in situ electrochemical cell set-up at MR-CAT beam-line of the APS, for x-ray reflectivity and x-ray fluorescence analysis of the SOFC oxygen electrodes.

2.2.3. Results and Discussion

Dense thin-film $La_{0.8}Sr_{0.2}MnO_{3+\delta}$ (LSM)Electrodes:

In order to enhance the sensitivity of the x-ray measurements to the surface and bulk of the electrode material, dense thin-film doped-lanthanum manganite model electrodes were analyzed in reflectivity geometry. Electrochemical activation during the cathodic and anodic dc polarization yielded significant improvement of the electrode performance. Therefore, we expect that the same phenomena can govern the electrochemical activation of both the porous electrodes and the idealized model dense thin-film electrodes. In fact, the dense film electrode can be viewed as representing a large-aspect ratio particle in the porous electrode. Figure 8 presents the typical electrochemical impedance spectra for the dense model electrodes. The EIS data is for a 150nm-thick electrode on single crystal YSZ electrolyte tested in the *ex situ* set-up before and after current-conditioning at -0.8V for 15 minutes. A high-frequency intercept that is influenced by current-conditioning only to a small extent, a low-frequency region main impedance arc that is significantly reduced in magnitude during current-conditioning, and multiple overlapping impedance arcs in intermediate-frequency regions after current-conditioning are observed. The intermediate-frequency impedance arc(s) relax back very slowly after the dc polarization is removed. In accordance with literature [12], this medium to low frequency region of the electrochemical impedance spectrum can be attributed to the oxide ion diffusion on the surface or the bulk of the LSM electrode and/or the surface exchange and reduction of oxygen on LSM. The transient activation of the electrode represented as the decrease in the total impedance was shown in Figure 2 and Figure 4 for 700°C. The x-ray measurements presented here are in accordance with the time dependence of electrochemical activation of the electrodes.

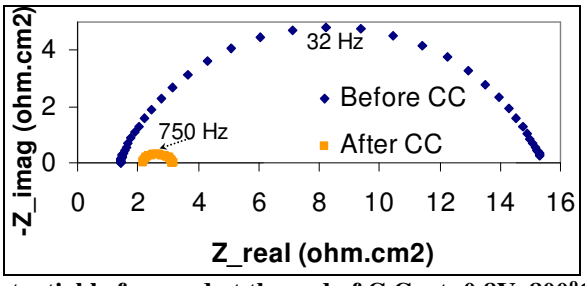

Figure 8: EIS at open circuit potential before and at the end of C.C. at -0.8V, 800°C for 15min for the 150nm-thick dense LCM electrode.

The electrochemical activation behavior of a 10nm-thick dense expitaxial LSM electrode on YSZ is presented in Figure 9. This electrode was tested *in situ* in the configuration shown in Figure 5 at the MR-CAT beamline. Each current conditioning (CC) period was accompanied by x-ray absorption spectroscopy measurements.

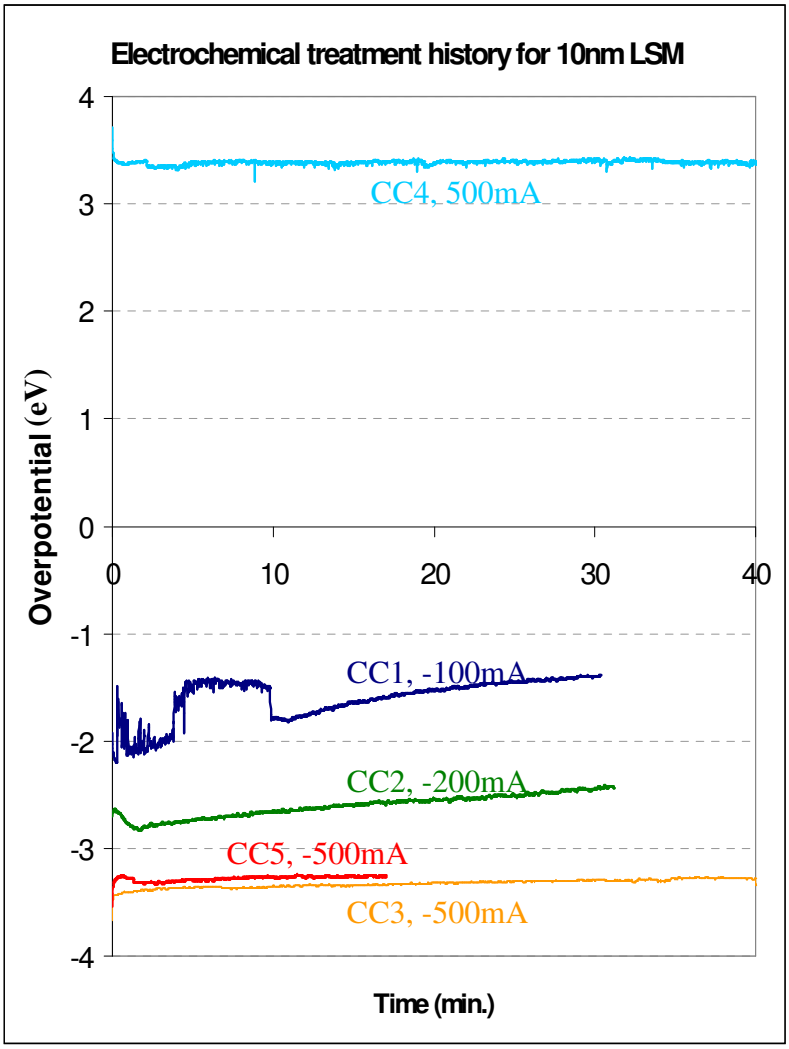

Figure 9: Electrochemical current conditioning (CC) history and activation behavior for the 10nm-thin epitaxial dense thin film electrode supported by YSZ electrolyte at 700°C tested in situ during x-ray measurements in the configuration shown in Figure 5.

X-ray reflectivity and x-ray fluorescence measurements were performed on the dense thin-film model electrodes under *in situ* conditions, i.e. at high temperature and under electrochemical dc polarization, to reveal the chemical and structural nature of electrode materials upon polarization. The current prevailing hypothesis for La-Sr based perovskite electrodes is that the A-site elements (La and Sr in this case) serve as unreactive supports for the crystal structure. Although it was never proven with *in situ* x-ray techniques, it is expected in the literature that B-site Mn surrounded by oxygen atoms must be changing its chemical state during polarization, such as during current-conditioning [13]. A change in the chemical state of Mn under electrical polarization can lead to a higher amount of oxygen vacancies or active sites in the manganite electrode, which can consequently improve the oxide ion diffusion or its surface exchange kinetics. In FY06, we obtained Mn K-edge X-ray absorption near edge spectra (XANES) of several LSM and LCM dense thin-film

electrodes of 20-200nm thickness on single-crystal yttria-stabilized zirconia (YSZ) electrolytes operating at 700-800°C under dc polarization. The Mn *K*-edge XANES measurements showed *no changes* for any of the dense thin-film doped lanthanum manganite electrode samples, either in the bulk or at the surface of the films, during the cathodic and anodic dc polarization-induced activation of the electrodes at high temperature. Thus, one of the intriguing findings of these studies is that the Mn oxidation state does not detectably change under polarization of the electrode, contrary to a theory postulated in the literature that cathodic polarization reduces Mn^{4+} to Mn^{3+}, or Mn^{3+} to Mn^{2+} [13], or visa versa for anodic polarization, resulting in the formation of oxygen vacancies on the electrode surface, in its bulk, or close to the interface with the YSZ electrolyte.

Nevertheless, some form of chemical change of the electrode material is likely to take place under electrochemical polarization. Therefore, the A-site component of the doped-lanthanum manganite was investigated in our study, in spite of the current prevailing hypothesis for La-based perovskite electrodes that the A-site elements are unreactive. In FY06, he La L_{III}-edge XANES behavior of several LSM model electrode samples was examined under cathodic and anodic dc polarization, at 700-800°C, using depth-sensitive glancing angle incidence for the XANES analysis. No change either in total fluorescence or in the La L_{III}-edge peak intensity was found when the measurement was performed at low angles probing the bulk of the electrode films, as shown in Figure 10-a. This indicates either that the A-site element, La, is not subject to a net change when all the electrode bulk is probed on average, or that the possible chemical changes are very localized such that the bulk measurement is not sufficiently sensitive to probe such localized changes. When the incidence angle was reduced to below the critical angle (~0.5° in our experiments), an increase in the total fluorescence as well as a decrease in the La L_{III}-edge peak intensity (white-line height) with the increasing degree of current-conditioning in oxygen-evolution polarization mode was observed. The overall fluorescence intensity is proportional to the concentration of La and the peak or white line intensity is sensitive to the electronic state of the La. An increase in the white-line intensity in the La L_{III} XANES indicates an increase in the number of electronic vacancies in the La 5d-band. A plot of the consequent changes in the La L_{III}-edge XANES corresponding to the surface of the LSM electrode films when anodic and open circuit potentials were repeatedly applied is shown in Figure 10-b. As seen in Figure 10-b, the La L_{III}-edge XANES changes with time under polarization approaching a steady-state trace with time. This stabilization of the La XANES data is correlated with stabilization of the area-specific resistance of the electrode, as presented in Figure 2. This effect was seen repeatedly on several independently measured doped-lanthanum manganite electrodes of 100nm and 150nm thickness.

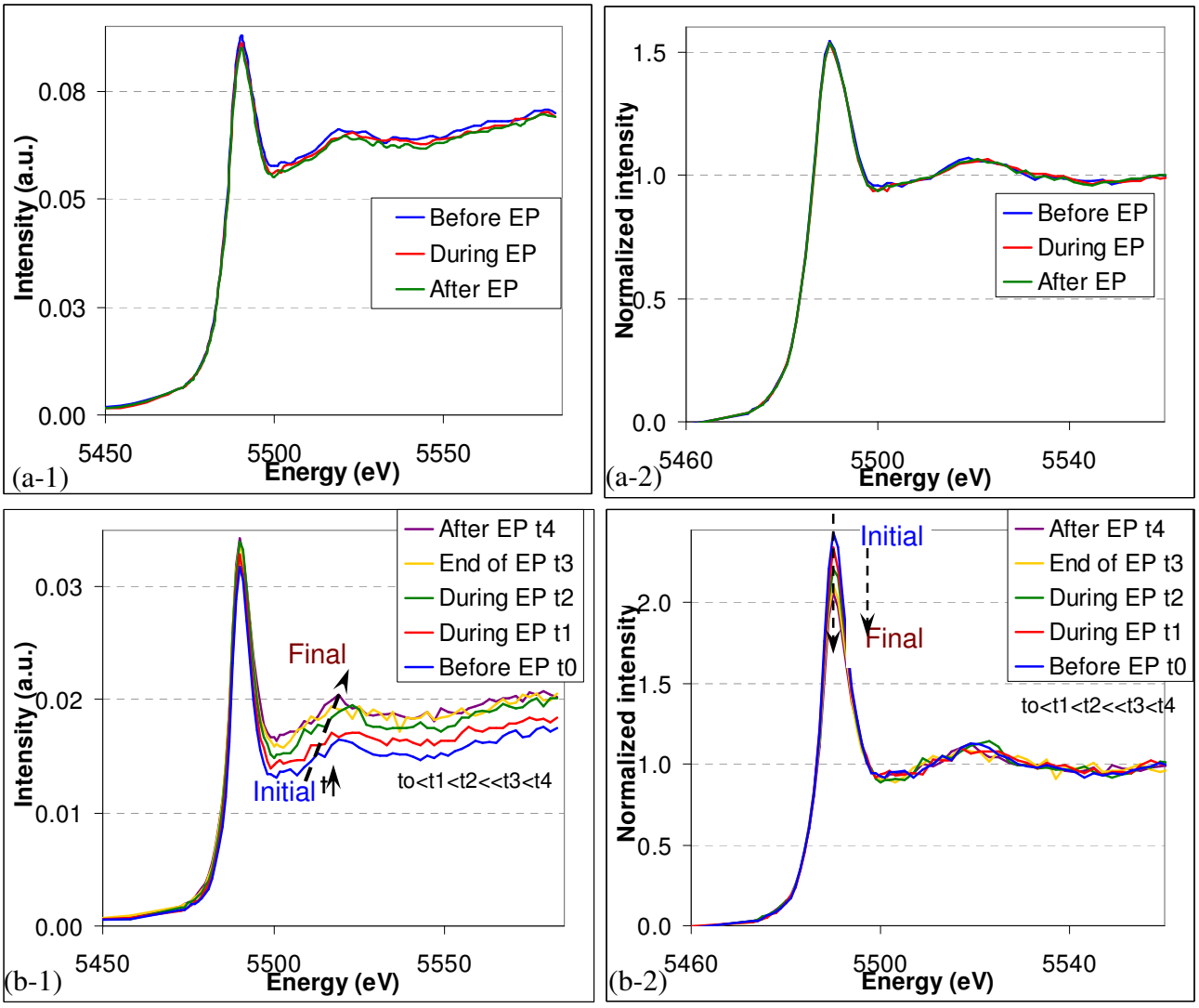

Figure 10: Grazing incidence angle XANES of La L_{III}-edge at 700°C (a) in the bulk of the dense thin-film LSM before, during, and after the anodic electrochemical polarization (EP) of 0.8V, (b) at the surface of the dense thin-film LSM before, during (at several consecutive times), and after the anodic electrochemical polarization (EP) of 0.8V. 1- Data normalized to show edge height (proportional to the concentration of La). 2-Data normalized to show changes in white-line intensity (proportional to d-band vacancy of La).

In FY07, we performed grazing incidence angle XANES measurements near Sr K-edge sensitive to the surface and bulk of the LSM dense electrode films, before, during and after electrochemical polarization treatments. Similarly, to La L_{III}-edge results at 700°C, chemical and compositional changes related to Sr were shown to evolve upon electrochemical polarization. Sr concentration was shown to increase only for incidence angles below the critical angle. The results indicated that the surface concentration of Sr increased only when the resistance of the electrode decreased (electrode activated) in oxygen reduction and in oxygen evolution mode (Figure 11-a) The surface composition change and the electrochemical activation remained upon removal of the current (transition from CC5 to OCP_l in Figure 9). This effect was seen repeatedly on several independently measured LSM electrodes of 10nm-150nm thickness. Additionally, the near-edge region appear to evolve also as a function of electrochemical current and activation, indicating chemical state changes related to Sr on the surface of LSM electrodes (Figure 11-b).

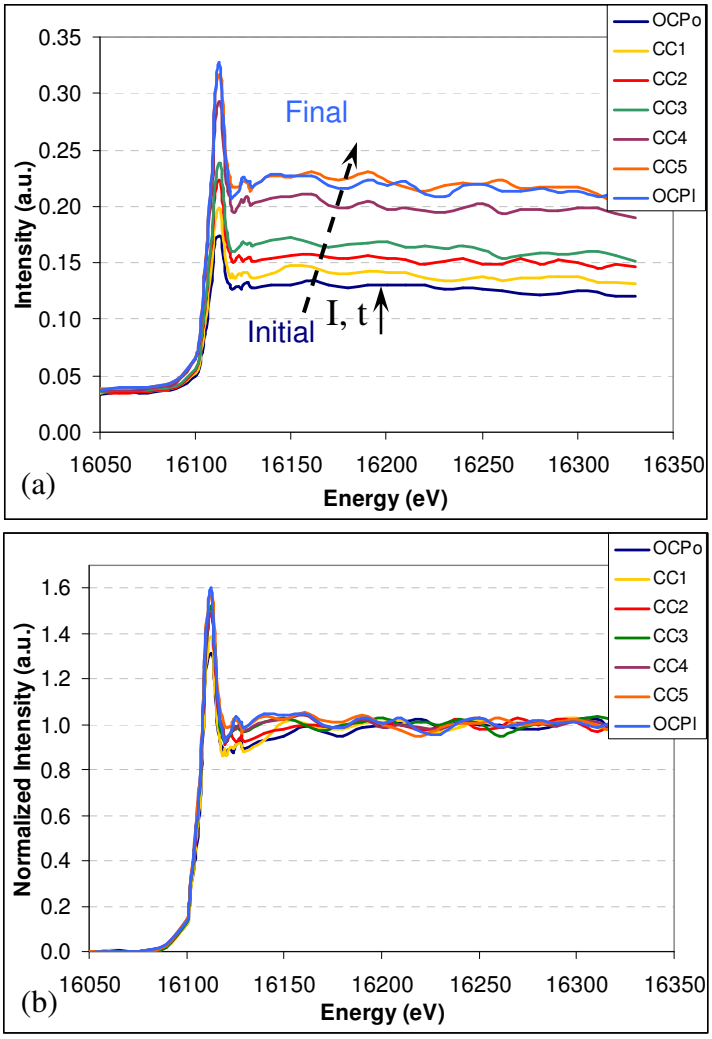

Figure 11: Grazing incidence angle XANES of Sr K-edge at 700°C at the surface of the dense thin-film LSM before (OCP_o), during(CC1,2,3,4,5), and after(OCP_l) the cathodic and anodic electrochemical polarizations (EP) (a) Data normalized to show total fluorescence intensity (proportional to the concentration of Sr). (b) Data normalized to show changes in near the K-edge. EP history of this electrode, for each current conditioning (CC) shown in these plots, is depicted in Figure 9. OCPl was measured 45min after CC5 ended.

The clear changes in the total fluorescence, the white-line intensity and near-edge region could be observed only when the x-ray incident angle was below the critical angle of reflectivity. This suggests that the increase in the concentration and the change in the electronic state of the La and Sr occurred only at the air-electrode interface. We found that Sr segregates to the surface upon passing current through the electrode and the cell, as long as there is electrochemical activation, in *both* the cathodic and anodic mode. While the electrochemical activation and surface concentration of Sr seemed irreversible for the very thin electrode films (10nm in Figure 9), the effect seemed reversible for thicker films (>~100nm). For example, Figure 12 shows the Sr-K edge XANES measurements on a 150nm-thick non-epitaxial LSM electrode upon anodic polarization followed by OCP conditions. A sharp increase in fluorescence is followed by a relatively fast decrease upon removal of the anodic current from the electrode. The difference in the residency of the electrochemical activation and surface concentration increase of Sr as a function of LSM film thickness will be subject to study in our studies.

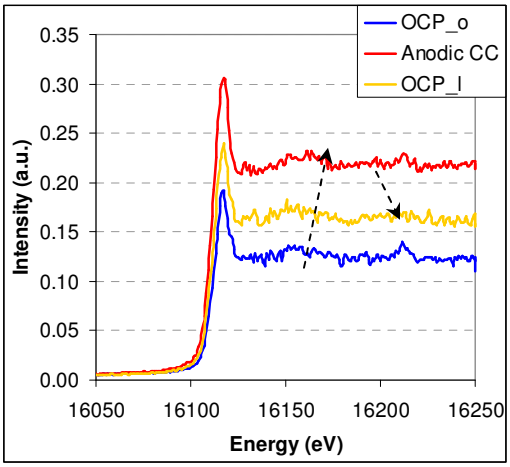

Figure 12: Grazing incidence angle XANES of Sr K-edge at 700°C at the surface of the dense thin-film LSM before (OCP_o), during (Anodic CC), and after (OCP_I) the electrochemical polarizations. Data normalized to show total fluorescence intensity (proportional to the concentration of Sr).

In addition, the anodic polarization and current conditioning has lead to a higher increase of Sr on the surface of the LSM electrodes, as seen in the transition from CC3 to CC4 in Figure 9. This is contrary to findings that show no changes on the surface concentration of Sr upon anodic polarization of $La_{0.6}Sr_{0.4}Co_{0.8}Fe_{0.2}O_3$ dense thin film electrodes [8]**[14]**. We think that the current leads to a kinetic effect and increases the mobility of cations, in this case Sr in LSM. The local PO_2 at the LSM surface, which is altered by oxygen reduction and evolution at the surface, may favor a higher concentration of Sr at the LSM surface as a new thermodynamic equilibrium **[15]**. The effects of both the current and the surface PO_2 can then lead to surface compositional changes that favor oxygen exchange kinetics causing improvement in electrochemical performance.

Our observation related to the role of the A-site cations' on the surface of LSM is unexpected and probably unique to the electrochemical current-conditioning. The results can imply an active role of both A-site elements, La and Sr, in oxygen surface chemisorption and charge transfer processes, and be related to the improved oxygen reaction rate, thus faster exchange of oxygen, *at the surface of the electrodes* in electrolysis cell anodes during electrochemical polarization. It is especially interesting that such a phenomenon can control the electrochemical activation of the doped-lanthanum manganite electrode, whose performance was thought to be limited by bulk diffusion of oxygen rather than by surface exchange of oxygen.

2.2.4. Future Work

In order to understand the role of electrode composition and chemical state at the surface, in the bulk and at the electrode-electrolyte interface on the initial and long-term electrochemical performance of SOEC anodes, we will continue to perform *in situ* x-ray characterization of model oxygen electrodes for SOECs, as a function of composition and crystal structure. The role of the dopant material (e.g. Sr) and the characteristics of the B-site materials in other perovskite electrode materials will be studied. In this way, we can identify and utilize the favorable compositions and chemical properties of the candidate electrode materials for more efficient and more durable SOECs for high temperature steam electrolysis.

3. Conclusions and Future Work

The governing reaction mechanisms, and the electrode and electrolyte material compositions and structures, that controls the efficiency and durability of the SOECs for high temperature steam electrolysis need to be identified and well-understood for a significant improvement in SOEC performance. In FY07, ANL conducted further experimental analysis of SOEC electrodes to progress in this objective.

Our effort on the oxygen electrode focused on specifically the effect of electrode crystal structure and morphology on its electrochemical performance, and the evolution of the electronic and structural properties of the electrodes while under electrochemical conditions and high temperature. We found through electrochemical impedance spectroscopy experiments that, indeed, different crystal orientations in a given oxygen electrode material, for example LSM, show different initial performance and different electrochemical activation under SOEC conditions. On the other hand, LSC which is a good mixed ionic and electronic conductor, did not exhibit a different electrochemical performance upon changing synthesis conditions. Our work in this area will continue to identify the optimal structures in manganite and cobaltite materials for higher oxygen surface exchange and bulk diffusion in SOEC electrodes.

Our *in-situ* x-ray and electrochemical measurements at the Advanced Photon Source of ANL have identified the chemical states of the main components of the doped lanthanum manganite electrodes. We found that the increase in the concentration and the change in the chemical state of the La and Sr (the A-site elements of the perovskite) occurring at the top air-electrode film interface can be responsible from the electrochemical improvement of the SOEC anode under DC current. Our observation related to the A-site chemical state change is unexpected and probably unique to the electrochemical current-conditioning. The results can imply an active role of A-site in oxygen surface chemisorption and charge transfer processes, and be related to the improved oxygen reaction rate, thus faster exchange of oxygen, *at the surface of the electrodes* in electrolysis cell anodes during electrochemical polarization. It is especially interesting that such a surface phenomenon can control the electrochemical activation of the doped-lanthanum manganite electrode, whose performance was thought to be limited by bulk diffusion of oxygen rather than by surface exchange of oxygen. In order to understand the role of electrode composition and chemical state at the surface, in the bulk and at the electrode-electrolyte interface on the initial and long-term electrochemical performance of SOEC anodes, we will continue to perform *in-situ* x-ray characterization of model oxygen electrodes for SOECs, as a function of composition and crystal structure. The irreversibility of the electrode activation in thinner films is of interest to future studies for identifying additional phases that may form on the electrode surface upon significant compositional changes. The role of the dopant materials and the characteristics of the B-site materials in other perovskite electrode materials will be studied. In this way, we can identify and utilize the favorable compositions and chemical properties of the candidate electrode materials for more efficient and more durable SOECs for high temperature steam electrolysis.

Acknowledgements

We thank Beihai Ma of ANL for facilitating the Pulsed laser deposition of LSM electrode samples, and Bruce Ravel for beamline support. MRCAT operations are supported by the Department of Energy (DOE) and the MRCAT member institutions.

References

[1] S. Singhal and K. Kendall, *High Temperature Solid Oxide Fuel Cells: Fundamentals, Design, and Applications*, (New York: Elsevier, 2003).
[2] Lee, H.Y., Cho, W.S., Oh, S.M., Wiemhofer, H.D., Gopel, W., *J. Electrochem. Soc.*, 1995, 142, 447.
[3] Kuznecov, M., Otschick, P., Obenaus, P., Eichler, K., Schaffrath, W., *Solid State Ionics*, 2004, 157, 371.
[4] Jiang, S.P., Love, J.G., *Solid State Ionics*, 2001, 138, 183.
[5] Martin, B.E., Proceedings of the Ninth International Symposium on SOFCs (SOFC IX) in the 207th Meeting of the Electrochemical Society, Quebec City, May 2005.
[6] Jiang, S.P., Wang, W., Proceedings of the Ninth International Symposium on SOFCs (SOFC IX) in the 207th Meeting of the Electrochemical Society, Quebec City, May 2005.
[7] Mitterdorfer, A., Gauckler, L.J., *Solid State Ionics*, 1998, 111, 185.
[8] Baumann, F.S., Fleig, J., Konuma, M., Starke, U., Habermeier, H-U., Maier, J., *J. Electrochem. Soc.*, 2005, 152, A2074.
[9] Nagy, Z., You, H., *Electrochim. Acta*, 2002, 47, 3037
[10] Mukerjee, S., Urian, R.C., *Electrochim. Acta*, 2002, 47, 3219
[11] Yildiz, B., la'O, G.J., Shaohorn, Y., submitted to the *J. Electrochem. Soc*.
[12] Adler, S.B., *Chem. Rev*., 2004, 104, 4791.
[13] Chen, X.J., Chan, S.H., Khor, K.A., *Electrochem. Solid-State Lett.*, 2004, 7, A144
[14] Baumann, F.S., "Oxygen reduction kinetics on mixed conducting SOFC model cathodes", Ph.D. Thesis, Max-Planck-Institut für Festkörperforschung, Stuttgart, 2006.
[15] Lein, H.L., Wiik, K., Grande, T., *Solid State Ionics*, 2006, 177, 1587.

Part II: Progress Towards the Atomic Layer Deposition of Lanthanum Strontium Manganate

Jeffrey W. Elam, David A. Honegger, Joseph A. Libera, and Michael. J. Pellin

ABSTRACT: Lanthanum strontium manganate (LSM) is the most commonly used cathode material for solid oxide fuel cells (SOFC) and also solid oxide electrolysis cells (SOEC) for hydrogen production through steam electrolysis. The ability to deposit LSM in the form of thin, conformal films onto high surface area support materials will enable the development of more efficient SOFC and SOEC devices. Moreover, thin, uniform LSM films prepared on flat surfaces are ideal for performing synchrotron X-ray experiments aimed at understanding the materials issues that control SOEC performance. Atomic layer deposition (ALD) is a very effective technology for fabricating thin, conformal films on flat surfaces as well as high surface area supports. In this study, we describe our work developing ALD methods for depositing La_2O_3, MnO_2, and mixtures of these oxides using cyclopentadienyl precursors. We have utilized *in situ* quartz crystal microbalance (QCM) measurements to explore the range of conditions for growth of these materials as well as to determine the appropriate oxygen sources. In addition, thin films of La_2O_3 and MnO_2 were deposited on Si(100) substrates and analyzed using spectroscopic ellipsometry to determine the refractive index and growth rates of these materials. Finally, mixed-oxide films La_2O_3 and MnO_2 were prepared and analyzed with X-ray fluorescence to determine the composition of the films.

1. Introduction

Atomic layer deposition (ALD) is a powerful method for applying precise, conformal coatings over nearly any substrate including nanoporous materials. ALD utilizes a binary reaction sequence of self-saturating chemical reactions between gaseous precursor molecules and a solid surface to deposit films in a monolayer-by-monolayer fashion. ALD can be used to deposit a wide range of materials, and the resulting films are typically dense, pinhole-free and extremely conformal. Lanthanum strontium manganate ($La_{1-x}Sr_xMnO_{3-d}$, LSM) is a common cathode material for solid oxide fuel cells (SOFC) and solid oxide electrolysis cells (SOEC). Typically, the composition used for LSM in SOFC/SOEC applications has x=0.15-0.3. The ALD of LSM requires separate procedures for depositing the individual component oxides: La_2O_3, SrO and MnO_2. In addition, the range of allowable growth temperatures for each of the component oxides must overlap. Finally, it must be possible to deposit each of the oxides on the other component oxides. All of these requirements make the ALD of multicomponent oxides such as LSM a challenging task. Because of this challenge, there has been only one example to date of a three-component oxide material deposited using ALD methods[1].

There has been previous work depositing La_2O_3 and MnO_2 using beta diketonate precursors by ALD [1, 2]. However, the beta diketonate precursors suffer from a number of restrictions including low volatility, low ALD growth rates, the requirement of high deposition temperatures, and the need for O_3 as an oxygen source. These restrictions limit the utility of these methods, particularly for coating nanoporous solids. Consequently, the strategy that we adopted in this project was to develop new methods utilizing cyclopentadienyl precursors. Typically, cyclopentadienyl precursors have high volatility, yield high growth rates at lower deposition temperatures, and are reactive with more stable oxygen sources such as water.

2. Experimental

The ALD films were deposited in a custom viscous flow reactor similar in design to those that have been described previously[3]. Briefly, a stainless steel flow tube with an inside diameter of 5 cm houses substrates for film growth as well as the quartz crystal microbalance (QCM). Ultrahigh purity nitrogen carrier gas continuously passes through the flow tube at a mass flow rate of 360 sccm and a pressure of 1 Torr. A constant reactor temperature is maintained by four separate temperature controllers connected to resistive heating elements attached to the outside of the reactor. The four heating zones create a uniform temperature profile along the length of the flow tube to reduce the

influence of temperature transients on the QCM measurements. All of the chemicals are introduced into the ALD reactor using pneumatic diaphragm valves.

MnO_2 ALD was performed using alternating exposures to Bis(ethylcyclopentadienyl) Manganese, ($Mn(EtCp)_2$, Strem, 98%) and deionized water while the La_2O_3 ALD used Tris(isopropylcyclopentadienyl) Lanthanum ($La(IpCp)_3$, Strem, 99.9%) and ozone. The $Mn(EtCp)_2$ and $La(IpCp)_3$ were held in a stainless steel bubblers maintained at 70 and 155°C, respectively, and the tubing connecting the bubblers to the ALD reactor was maintained at 200°C to prevent the condensation of the organometallic compounds on the reactor walls. The ALD was typically performed using a reactor temperature of 225°C. Ultrahigh purity nitrogen (99.999%) at a mass flow rate of 60 sccm was sent through the appropriate $Mn(EtCp)_2$ or $La(IpCp)_3$ bubblers during the organometallic exposures, and was diverted to bypass the bubblers following the organometallic exposures. The deionized water was held in a stainless steel reservoir maintained at room temperature and a metering valve was used to adjust the water flow rate to be ~40 sccm during the water exposures. The ozone was produced using a commercial ozone generator (Ozone Engineering L11) using a feed of ultrahigh purity oxygen at a flow rate of 400 sccm to produce ~10% ozone in oxygen.

The ALD timing sequences can be expressed as t1-t2-t3-t4 where t1 is the exposure time for the first precursor, t2 is the purge time following the first exposure, t3 is the exposure time for the second precursor, t4 is the purge time following the exposure to the second precursor and all units are given in seconds (s). The timing sequences for the La_2O_3 and the MnO_2 ALD were typically 1-5-3-5 s and 1-5-1-5 s, respectively. The composition of the La_2O_3-MnO_2 mixed oxide films was controlled by adjusting the relative number of La_2O_3 and MnO_2 ALD cycles during the course of the mixed oxide film growth.

A QCM was installed in the ALD reactor in place of substrates enabling *in situ* measurements during the ALD [3]. These measurements utilized a Maxtek BSH-150 bakeable sensor and AT-cut quartz sensor crystals with a polished front surface obtained from the Colorado Crystal Corporation, part # CCAT1BK-1007-000. The QCM measurements were made using a Maxtek TM400 film thickness monitor interfaced to a personal computer.

ALD films were deposited on 2 cm x 1 cm Si(100) substrates. Prior to loading, the substrates were ultrasonically cleaned in acetone and then isopropanol and blown dry using nitrogen. After loading, the substrates were allowed to outgas in the ALD reactor for 10 minutes at 225°C in 1 Torr of flowing ultrahigh purity nitrogen. Next, the substrates were cleaned *in situ* using a 60 s exposure

to 10 % ozone in oxygen at a total pressure of 2 Torr and a mass flow rate of 400 sccm. La_2O_3 films are hygroscopic and can absorb atmospheric water to form lanthanum hydroxide, and this effect can complicate the analysis of the films. To prevent the formation of lanthanum hydroxide, the La_2O_3 films were first capped with a 62 nm layer of ALD Al_2O_3 prior to removal from the ALD reactor. The ALD Al_2O_3 was performed using 50 cycles of trimethyl aluminum/H_2O with the timing sequence 1-5-1-5.

Ellipsometric measurements of the ALD films deposited on Si(100) surfaces were performed using a J. A. Woolam Co. M2000 variable angle spectroscopic ellipsometer (VASE). These measurements determined the thickness and refractive index of the films. X-ray fluorescence (XRF) analysis of the YSZ films was performed using an Oxford Instruments ED2000 to determine the relative La and Mn contents of the films.

3. Results and Discussion

A) Growth of MnO_2 Films

To determine the appropriate oxygen source for MnO_2 ALD, *in situ* QCM measurements were performed. Figure 1 shows the QCM measurements recorded during alternating $Mn(EtCp)_2/H_2O$ exposures with the timing sequence 1-5-1-5 at a deposition temperature of 250°C and a bubbler temperature of 70°C. These measurements assumed that the MnO_2 deposits at the bulk density of 5.03 g/cc. Figure 1a reveals sustained, linear growth at a growth rate of 0.7 Å/cycle. Figure 1b shows an expanded view of the MnO_2 ALD illustrating the step structure of the QCM data. The mass increase observed during the H_2O exposures suggests that a majority of the EtCp ligands are removed during the $Mn(EtCp)_2$ exposures [4]. Additional measurements performed using O_3 as the oxygen source failed to yield sustained MnO_2 growth indicating that O_3 is not a suitable oxygen source under these growth conditions.

Figure 2 shows the results of varying the $Mn(EtCp)_2$ bubbler temperature for a series of MnO_2 films deposited using 100 cycles of $Mn(EtCp)_2/H_2O$ with the timing sequence 1-5-1-5 on Si(100) at a deposition temperature of 150°C. The growth rates determined from VASE measurements remain constant for bubbler temperatures above ~70°C demonstrating that sufficient precursor is vaporized under these conditions to saturate all of the available reactive surfaces and ensure layer-by-layer growth. For most of the remaining experiments using the $Mn(EtCp)_2$ precursor, a bubbler temperature of 70°C was utilized.

Next, we examined the influence of the deposition temperature on the MnO_2 growth. The MnO_2 growth rate decreases from 1.34 Å/cycle at 100°C to 0.80 Å /cycle at 300°C as shown in

Figure 3. This decrease in growth rate probably results from a decrease in the concentration of surface hydroxyl groups at higher temperatures as a result of the condensation reaction [5]:

$$2\ MnOH \rightarrow Mn\text{-}O\text{-}Mn + H_2O$$

The lower concentration of surface hydroxyls will result in fewer adsorption sights for the $Mn(EtCp)_2$ precursor and a lower ALD growth rate. The growth rate of 0.83 Å/cycle at 250°C obtained from the ellipsometric measurements is close to the growth rate of 0.7 Å/cycle measured using the QCM assuming a bulk density of 5.03 g/cc. This similarity indicates that the MnO_2 is depositing as a dense film.

A series of MnO_2 films was prepared on Si(100) using increasing numbers of $Mn(EtCp)_2/H_2O$ cycles at 150°C and the thicknesses of these films determined using VASE measurements are shown in Figure 4. The MnO_2 growth is extremely linear at a growth rate of 1.09 Å/cycle, and the growth rate is nearly constant even for the thinnest MnO_2 films indicating rapid nucleation on the native oxide surface of the Si(100) substrate. The refractive index determined from the thickest MnO_2 film prepared using 500 ALD cycles is n=2.16 at 633 nm. This value agrees well with previous measurements for MnO_2 thin films prepared by thermal evaporation [6].

B) Growth of La_2O_3 Films

For the initial La_2O_3 experiments, *in situ* QCM measurements were performed to evaluate possible oxygen sources. These measurements revealed that H_2O was not suitable because alternating $La(IpCp)_3/H_2O$ failed to yield sustained growth, while O_3 did allow La_2O_3 growth. Figure 5a shows QCM measurements recorded using alternating $La(IpCp)_3/O_3$ exposures using the timing sequence 1-5-3-5 at a deposition temperature of 250°C using a $La(IpCp)_3$ bubbler temperature of 220°C and yields a growth rate of 0.49 Å/cycle. Figure 5b illustrates the step structure observed by the QCM during the La_2O_3 ALD. The net mass decrease observed following the O_3 exposures is consistent with the removal of a large fraction of IpCp ligands by the O_3 and indicates that these ligands remain on the surface after $La(IpCp)_3$ exposures. This large coverage of IpCp ligands following the $La(IpCp)_3$ exposures will prevent the adsorption of additional $La(IpCp)_3$ molecules and partially explains the relatively low La_2O_3 growth rate of 0.49 Å/cycle.

Figure 6 shows the results of *in situ* QCM measurements recorded during the ALD of La_2O_3 films using alternating exposures to $La(IpCp)_3/O_3$ at a temperature of 225°C using the timing sequence x-5-3-5 in which the $La(IpCp)_3$ exposure time is varied between 0.25 and 2 seconds. This figure demonstrates that the La_2O_3 ALD is self limiting and the growth rate is nearly saturated at

~0.5 Å/cycle for $La(IpCp)_3$ exposure times exceeding 0.5 s. Additional QCM measurements were performed to verify that the O_3 exposure time of 3 s is sufficient to saturate the La_2O_3 growth.

Next, a series of La_2O_3 films were prepared on Si(100) surfaces at a temperature of 225°C using increasing numbers of $La(IpCp)_3/O_3$ cycles. The thicknesses of these films were determined using VASE and the results of these measurements are shown in Figure 7. The La_2O_3 ALD process yields a growth rate of 0.86 Å/cycle, and the growth rate is nearly constant versus the number of ALD cycles indicating that there is no inhibition or incubation period for the La_2O_3 growth on the Si(100) native oxide surface. The VASE measurements yield a refractive index of n=1.82 at 633 nm for the thickest, 43 nm La_2O_3 film. This value agrees well with previous measurements of La_2O_3 thin films [7]. The discrepancy between the growth rate value of 0.86 Å/cycle obtained using VASE and 0.49 Å/cycle obtained using the QCM may indicate that the La_2O_3 films are deposited at a lower density than the assumed bulk density of 6.51 g/cc used to calibrate the QCM measurements. Alternatively, these differences may stem from the fact that the QCM is located ~10 cm away from the sample placement location in the ALD reactor. Additional La_2O_3 ALD experiments will evaluate this discrepancy.

B) Growth of MnO_2/La_2O_3 Mixed Oxide Films

Our initial examination of the MnO_2/La_2O_3 mixed oxide films utilized QCM measurements to investigate the necessary growth conditions for these materials. These experiments were performed using a deposition temperature of 225°C and bubbler temperatures of 155°C and 70°C for the $La(IpCp)_3$ and $Mn(EtCp)_2$, respectively. Our results from depositing the individual component oxides demonstrated that only H_2O is effective for MnO_2 ALD and only O_3 is effective for La_2O_3 ALD. Based on these results, we attempted to deposit a mixed oxide film using the reactant sequence: $Mn(EtCp)_2/H_2O/La(IpCp)_3/O_3$. Surprisingly, this precursor sequence did not yield sustained growth as illustrated by the lower curve in Figure 8. However, we did observe sustained growth by reversing the oxygen precursors and using the reactant sequence: $Mn(EtCp)_2/O_3/La(IpCp)_3/H_2O$ as shown by the upper trace in Figure 8. This unexpected result suggests that the role of the oxygen source is not merely to remove the ligands from the preceding metal precursor exposure, but also to prepare the surface for the following metal precursor. For instance, because O_3 is required to deposit the pure La_2O_3 films using the $La(IpCp)_3$ precursor, an O_3 exposure is needed prior to the $La(IpCp)_3$ exposure when depositing the mixed oxide film. To our

knowledge, this interesting behavior has not been observed previously for the ALD of mixed oxide films.

Next, we proceeded to deposit a series of MnO_2/La_2O_3 mixed oxide films in which the relative number of MnO_2 and La_2O_3 ALD cycles was adjusted to control the composition of the resulting films. These films were deposited on Si(100) substrates using a deposition temperature of 225°C and bubbler temperatures of 155°C and 70°C for the $La(IpCp)_3$ and $Mn(EtCp)_2$, respectively. The MnO_2 and La_2O_3 contents of the films were determined using XRF measurements. The Mn and La XRF signals were calibrated using a series of pure MnO_2 and La_2O_3 films prepared on Si(100) for which the thicknesses were determined by VASE. The filled circles in Figure 9 show the MnO_2 weight percentages for the mixed oxide films determined from the XRF measurements. The solid line shows the expected MnO_2 content predicted by the densities and growth rates of the component oxide films. The close correspondence between the predicted and measured MnO_2 weight percent values indicates that the MnO_2 and La_2O_3 deposit at nearly the same rate in the mixed oxide films as in the pure oxide films. The primary goal of this project is to develop ALD methods for depositing thin films of LSM for SOFC/SOEC applications in which the composition should be: $La_{1-x}Sr_xMnO_{3-d}$ with x=0.15-0.3. To achieve x=0.2, this requires a MnO_2 weight percent of 48.5%, and from Figure 9, this requires a percentage of MnO_2 cycles of 40%.

4. Future Work

The first task to complete our project will be to finish the study of the MnO_2/La_2O_3 mixed oxide films by preparing and characterizing additional films spanning the complete range of MnO_2 weight percents. Next, we will develop an ALD method for depositing SrO. As a first step, we have acquired a new cyclopentadienyl compound for SrO ALD, Bis(pentamethylcyclopentadienyl) Strontium. By combining the methods for the three component oxides, MnO_2, La_2O_3, and SrO, we will fabricate and characterize the trimetallic mixed oxide films to achieve the appropriate LSM composition.

References

[1] O. Nilsen, E. Rauwel, H. Fjellvag, A. Kjekshus, J. Mater. Chem. 17 (2007) 1466.
[2] O. Nilsen, M. Peussa, H. Fjellvag, L. Niinisto, A. Kjekshus, J. Mater. Chem. 9 (1999) 1781.
[3] J.W. Elam, M.D. Groner, S.M. George, Reviews of Scientific Instruments 73 (2002) 2981.
[4] A. Rahtu, T. Alaranta, M. Ritala, Langmuir 17 (2001) 6506.
[5] A.W. Ott, J.W. Klaus, J.M. Johnson, S.M. George, Thin Solid Films 292 (1997) 135.

[6] M.F. Al-Kuhaili, Journal Of Vacuum Science & Technology A 24 (2006) 1746.
[7] W.M. He, S. Schuetz, R. Solanki, J. Belot, J. McAndrew, Electrochemical And Solid State Letters 7 (2004) G131.

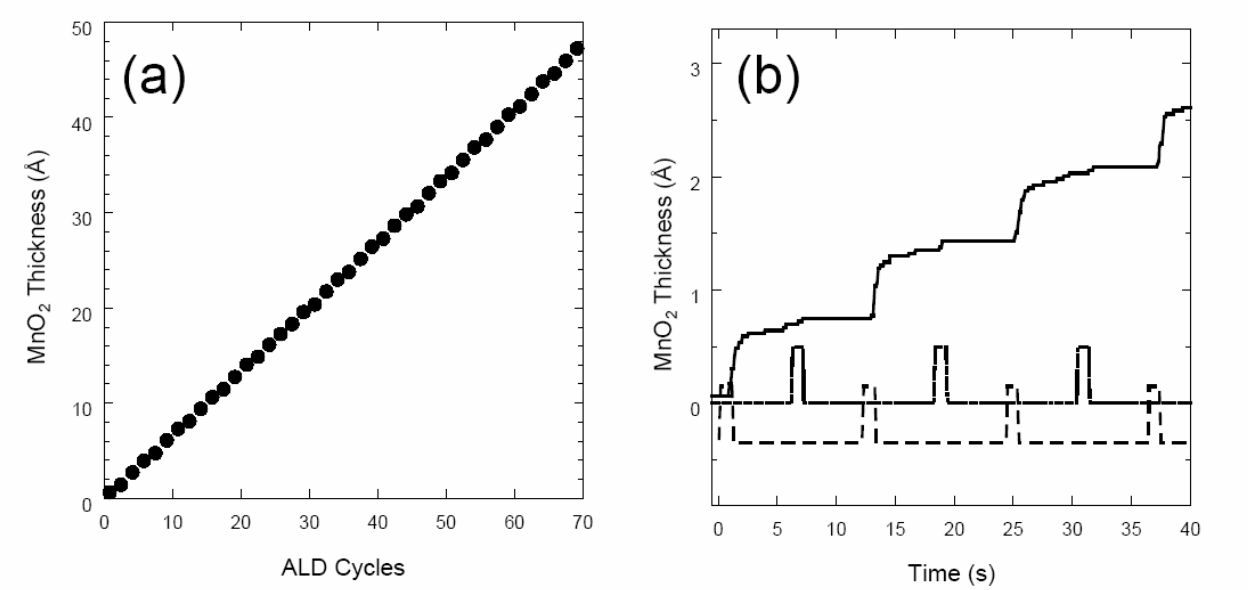

Figure 1

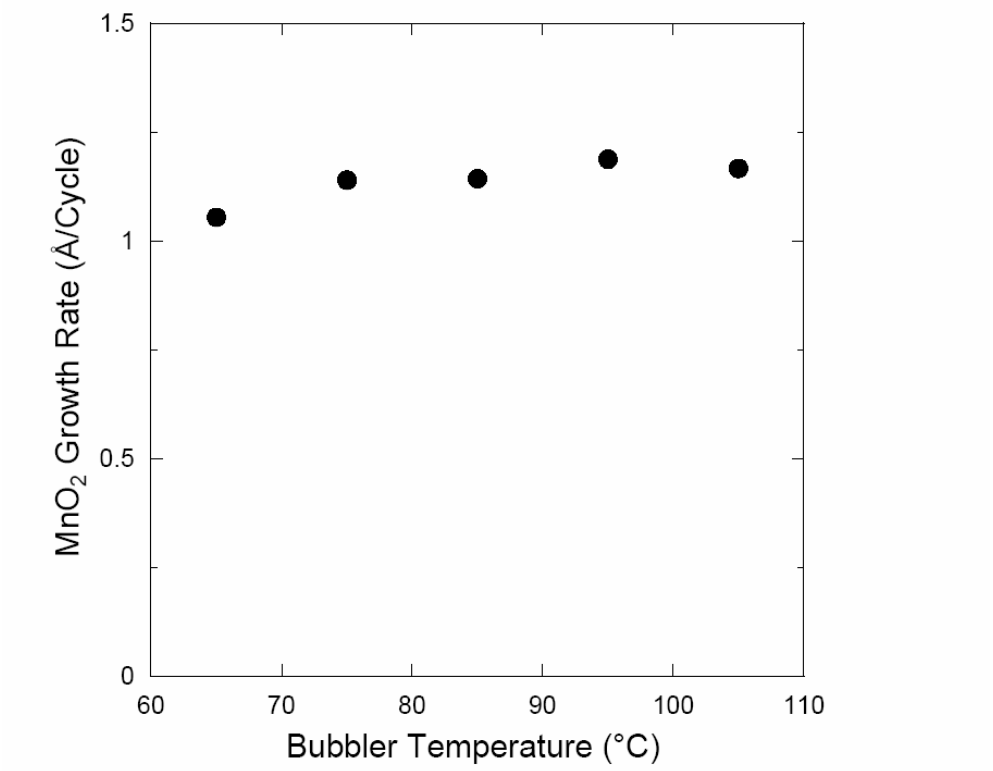

Figure 2

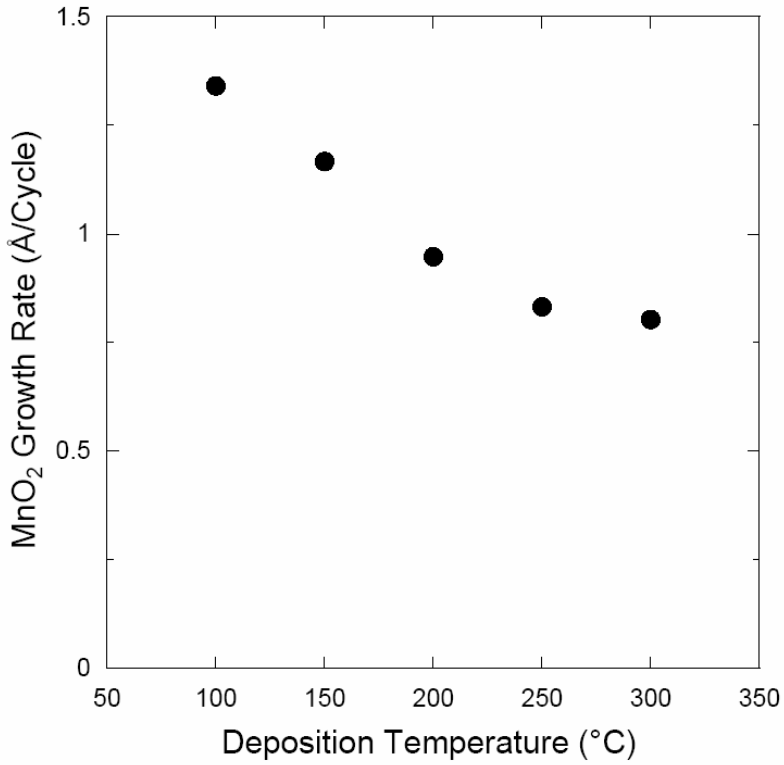

Figure 3

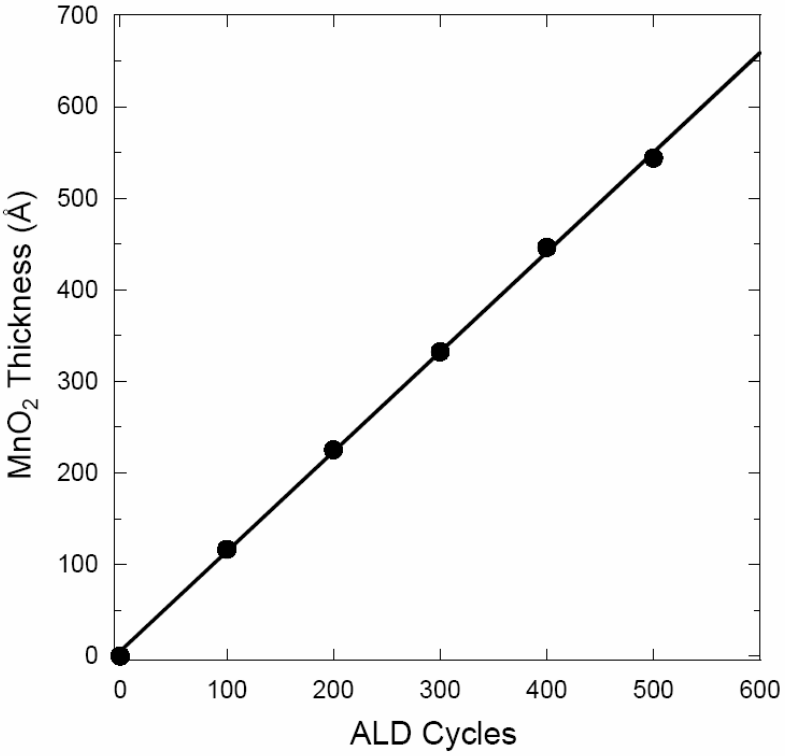

Figure 4

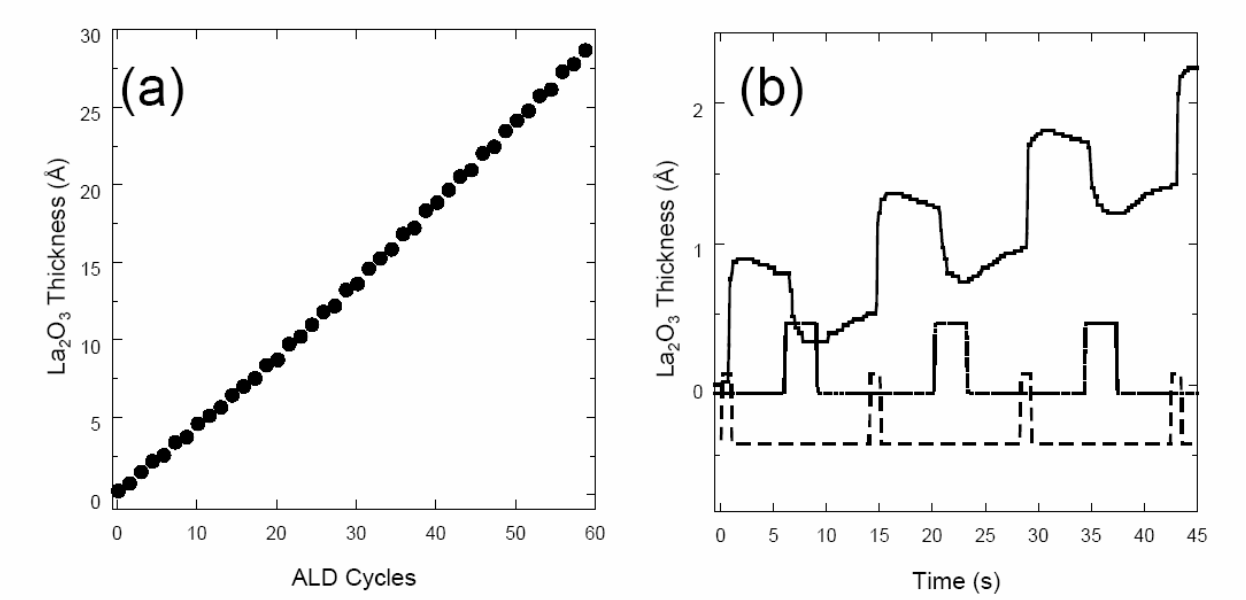

Figure 5

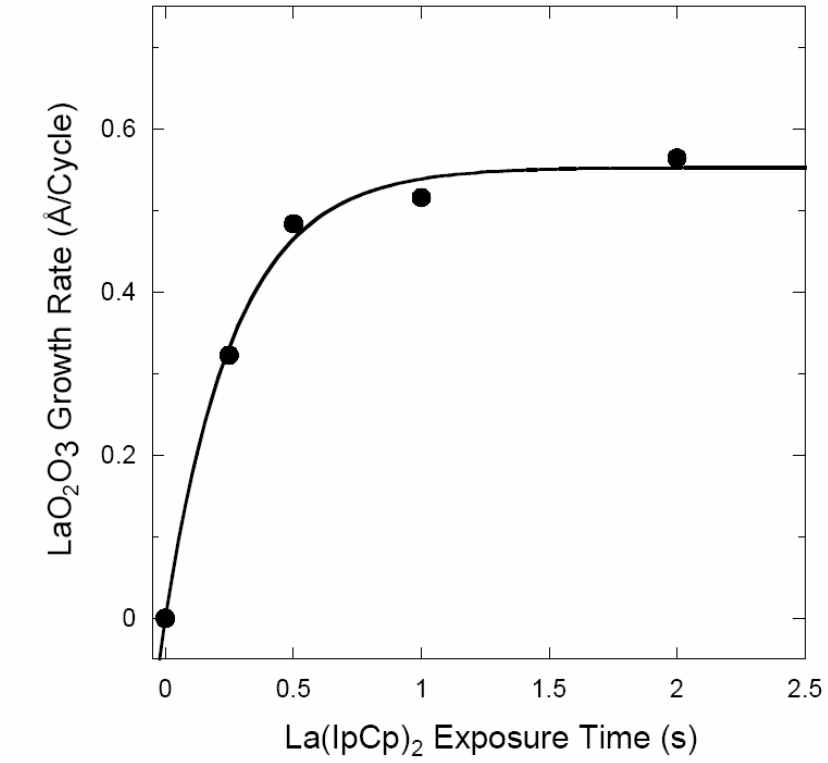

Figure 6

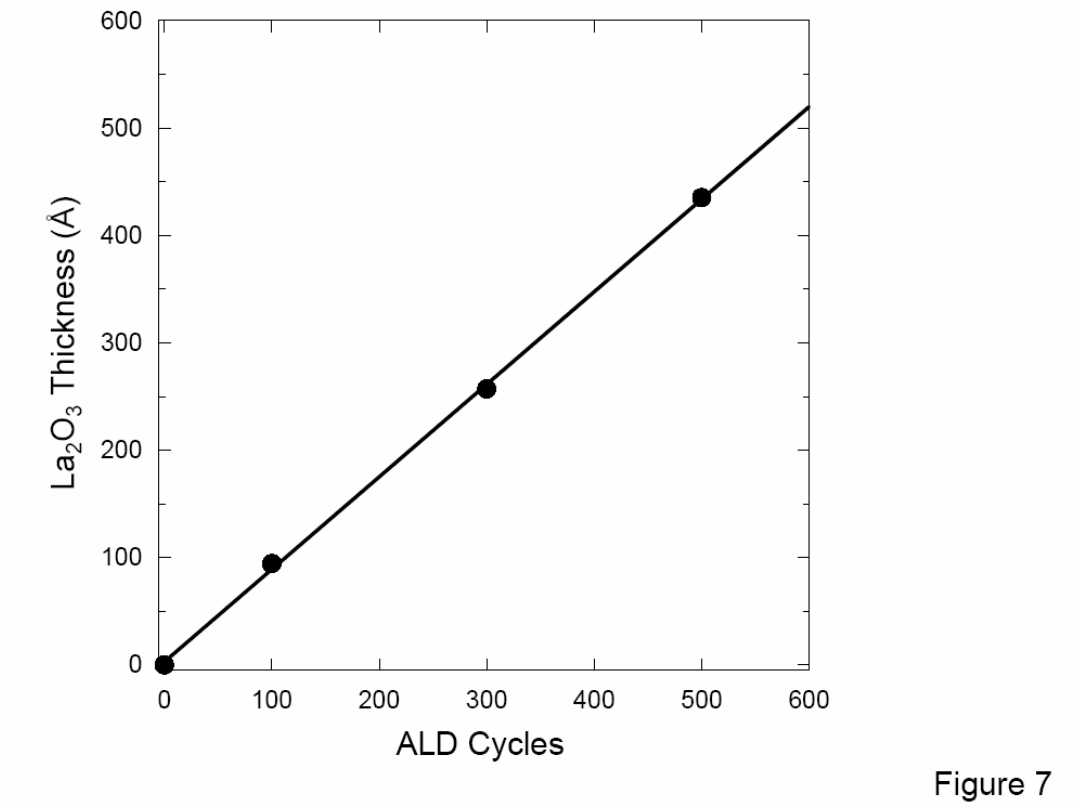

Figure 7

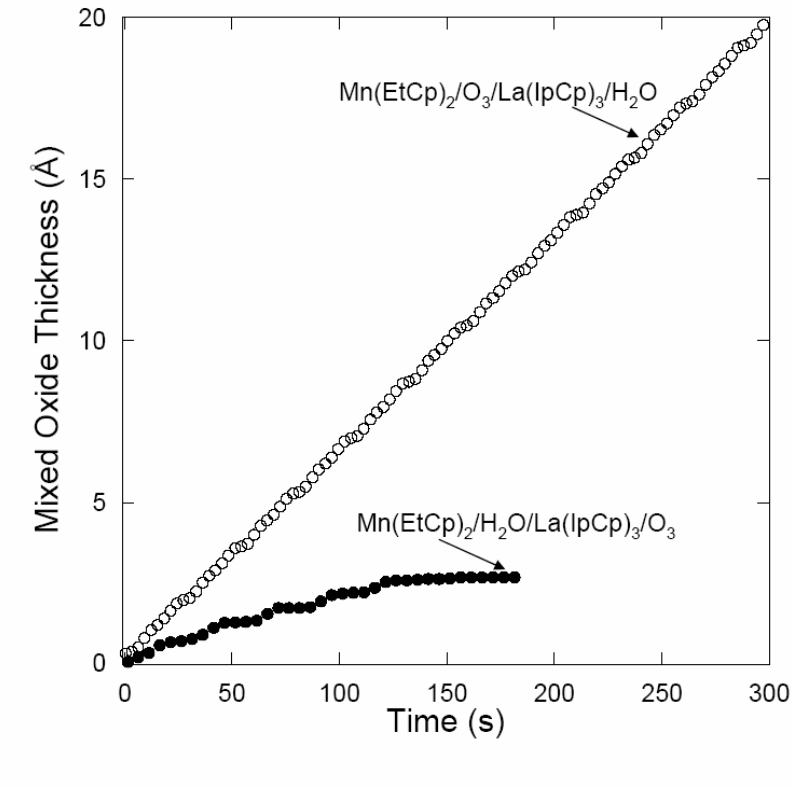

Figure 8

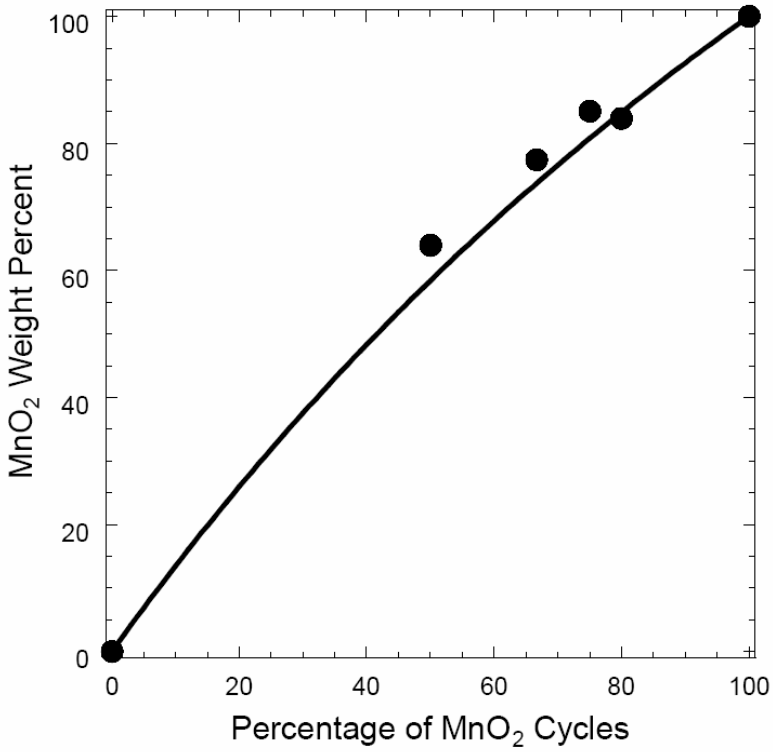
100
80
60
40
20
0
MnO_2 Weight Percent
0
20
40
60
80
100
Percentage of MnO_2 Cycles

Figure 9

Nuclear Engineering Division
Argonne National Laboratory
9700 South Cass Avenue, Bldg. 208
Argonne, IL 60439-4842

www.anl.gov

UChicago ▶ Argonne LLC

A U.S. Department of Energy laboratory
managed by UChicago Argonne, LLC